

# Longitudinal and transverse coupling in infrared gold nanoantenna arrays: long range versus short range interaction regimes

Daniel Weber,<sup>1,\*</sup> Pablo Albella,<sup>2</sup> Pablo Alonso-González,<sup>3</sup> Frank Neubrech,<sup>1</sup> Han Gui,<sup>4</sup> Tadaaki Nagao,<sup>4</sup> Rainer Hillenbrand,<sup>3,5</sup> Javier Aizpurua,<sup>2</sup> and Annemarie Pucci<sup>1</sup>

<sup>1</sup>Kirchhoff Institute for Physics, University of Heidelberg, Im Neuenheimer Feld 227, 69120 Heidelberg, Germany  
<sup>2</sup>Center for Materials Physics CSIC-UPV/EHU and Donostia International Physics Center, P. Manuel Lardizabal 5, San Sebastián-Donostia 20018, Spain

<sup>3</sup>Nanooptics Group, CIC nanoGUNE Consolider, Tolosa Hiribidea 76, San Sebastián-Donostia 20018, Spain

<sup>4</sup>World Premier International (WPI) Research Center for Materials Nanoarchitectonics (MANA), National Institute for Materials Science (NIMS), 1-1 Namiki, Tsukuba, Ibaraki, 305-0044, Japan

<sup>5</sup>IKERBASQUE, Basque Foundation for Science, Bilbao 48011, Spain

\*dweber@kip.uni-heidelberg.de

**Abstract:** Interaction between micrometer-long nanoantennas within an array considerably modifies the plasmonic resonant behaviour; for fundamental resonances in the infrared already at micrometer distances. In order to get systematic knowledge on the relationship between infrared plasmonic resonances and separation distances  $d_x$  and  $d_y$  in longitudinal and transverse direction, respectively, we experimentally studied the optical extinction spectra for rectangularly ordered lithographic gold nanorod arrays on silicon wafers. For small  $d_y$ , strong broadening of resonances and strongly decreased values of far-field extinction are detected which come along with a decreased near-field intensity, as indicated by near-field amplitude maps of the interacting nanoantennas. In contrast, near-field interaction over small  $d_x$  does only marginally broaden the resonance. Our findings set a path for optimum design of rectangular nanorod lattices for surface enhanced infrared spectroscopy.

©2011 Optical Society of America

**OCIS codes:** (300.6340) Spectroscopy: Spectroscopy, infrared; (240.6680) Optics at surfaces: Surface plasmons; (250.5403) Optoelectronics: Plasmonics; (260.3910) Physical optics: Metal optics.

---

## References and links

1. S. A. Maier and H. A. Atwater, "Plasmonics: Localization and guiding of electromagnetic energy in metal/dielectric structures," *J. Appl. Phys.* **98**(1), 011101 (2005).
2. M. Pelton, J. Aizpurua, and G. Bryant, "Metal-nanoparticle plasmonics," *Laser Photon. Rev.* **2**(3), 136–159 (2008).
3. D. Enders and A. Pucci, "Surface enhanced infrared absorption of octadecanethiol on wet-chemically prepared Au nanoparticle films," *Appl. Phys. Lett.* **88**(18), 184104 (2006).
4. F. Le, D. W. Brandl, Y. A. Urzhumov, H. Wang, J. Kundu, N. J. Halas, J. Aizpurua, and P. Nordlander, "Metallic nanoparticle arrays: a common substrate for both surface-enhanced Raman scattering and surface-enhanced infrared absorption," *ACS Nano* **2**(4), 707–718 (2008).
5. F. Neubrech, A. Pucci, T. W. Cornelius, S. Karim, A. García-Etxarri, and J. Aizpurua, "Resonant plasmonic and vibrational coupling in a tailored nanoantenna for infrared detection," *Phys. Rev. Lett.* **101**(15), 157403 (2008).
6. C. S. Levin, J. Kundu, A. Barhoumi, and N. J. Halas, "Nanoshell-based substrates for surface enhanced spectroscopic detection of biomolecules," *Analyst (Lond.)* **134**(9), 1745–1750 (2009).
7. A. Pucci, F. Neubrech, D. Weber, S. Hong, T. Toury, and M. L. de la Chapelle, "Surface enhanced infrared spectroscopy using gold nanoantennas," *Phys. Stat. Solidi B* **247**(8), 2071–2074 (2010).
8. R. Aroca, *Surface-enhanced Vibrational Spectroscopy* (John Wiley & Sons, 2006).
9. J. Grand, M. L. de la Chapelle, J.-L. Bijeon, P.-M. Adam, A. Vial, and P. Royer, "Role of localized surface plasmons in surface-enhanced Raman scattering of shape-controlled metallic particles in regular arrays," *Phys. Rev. B* **72**(3), 033407 (2005).
10. L. Billot, M. Lamy de la Chapelle, A. S. Grimault, A. Vial, D. Barchiesi, J. L. Bijeon, P. M. Adam, and P. Royer, "Surface enhanced Raman scattering on gold nanowire arrays: evidence of strong multipolar surface plasmon resonance enhancement," *Chem. Phys. Lett.* **422**(4–6), 303–307 (2006).

11. S. Lal, N. K. Grady, J. Kundu, C. S. Levin, J. B. Lassiter, and N. J. Halas, "Tailoring plasmonic substrates for surface enhanced spectroscopies," *Chem. Soc. Rev.* **37**(5), 898–911 (2008).
12. S. Nie and S. R. Emory, "Probing single molecules and single nanoparticles by surface-enhanced Raman scattering," *Science* **275**(5303), 1102–1106 (1997).
13. K. Kneipp, Y. Wang, H. Kneipp, L. T. Perelman, I. Itzkan, R. R. Dasari, and M. S. Feld, "Single molecule detection using surface-enhanced Raman scattering (SERS)," *Phys. Rev. Lett.* **78**(9), 1667–1670 (1997).
14. J. Kneipp, H. Kneipp, and K. Kneipp, "SERS—a single-molecule and nanoscale tool for bioanalytics," *Chem. Soc. Rev.* **37**(5), 1052–1060 (2008).
15. F. Neubrech, T. Kolb, R. Lovrincic, G. Fahsold, A. Pucci, J. Aizpurua, T. W. Cornelius, M. E. Toimil-Molares, R. Neumann, and S. Karim, "Resonances of individual metal nanowires in the infrared," *Appl. Phys. Lett.* **89**(25), 253104 (2006).
16. F. Neubrech, D. Weber, R. Lovrincic, A. Pucci, M. Lopes, T. Toury, and M. L. de la Chapelle, "Resonances of individual lithographic gold nanowires in the infrared," *Appl. Phys. Lett.* **93**(16), 163105 (2008).
17. G. W. Bryant, F. J. García de Abajo, and J. Aizpurua, "Mapping the plasmon resonances of metallic nanoantennas," *Nano Lett.* **8**(2), 631–636 (2008).
18. L. Novotny, "Effective wavelength scaling for optical antennas," *Phys. Rev. Lett.* **98**(26), 266802 (2007).
19. F. Neubrech, A. García-Etxarri, D. Weber, J. Bochlerle, H. Shen, M. Lamy de la Chapelle, G. W. Bryant, J. Aizpurua, and A. Pucci, "Defect-induced activation of symmetry forbidden infrared resonances in individual metallic nanorods," *Appl. Phys. Lett.* **96**(21), 213111 (2010).
20. R. Adato, A. A. Yanik, C.-H. Wu, G. Shvets, and H. Altug, "Radiative engineering of plasmon lifetimes in embedded nanoantenna arrays," *Opt. Express* **18**(5), 4526–4537 (2010).
21. K.-H. Su, Q.-H. Wei, X. Zhang, J. J. Mock, D. R. Smith, and S. Schultz, "Interparticle coupling effects on plasmon resonances of nanogold particles," *Nano Lett.* **3**(8), 1087–1090 (2003).
22. T. Atay, J.-H. Song, and A. V. Nurmikko, "Strongly interacting plasmon nanoparticle pairs: from dipole-dipole interaction to conductively coupled regime," *Nano Lett.* **4**(9), 1627–1631 (2004).
23. P. Nordlander, C. Oubre, E. Prodan, K. Li, and M. I. Stockman, "plasmon hybridization in nanoparticle dimers," *Nano Lett.* **4**(5), 899–903 (2004).
24. P. K. Jain, W. Huang, and M. A. El-Sayed, "On the universal scaling behavior of the distance decay of plasmon coupling in metal nanoparticles pairs: a plasmon ruler equation," *Nano Lett.* **7**(7), 2080–2088 (2007).
25. M. Gluodenis and C. A. Foss, "The effect of mutual orientation on the spectra of metal nanoparticle rod-rod and rod-sphere pairs," *J. Phys. Chem. B* **106**(37), 9484–9489 (2002).
26. A. M. Funston, C. Novo, T. J. Davis, and P. Mulvaney, "Plasmon coupling of gold nanorods at short distances and in different geometries," *Nano Lett.* **9**(4), 1651–1658 (2009).
27. D. P. Fromm, A. Sundaramurthy, P. J. Schuck, G. Kino, and W. E. Moerner, "Gap-dependent optical coupling of single "bowtie" nanoantennas resonant in the visible," *Nano Lett.* **4**(5), 957–961 (2004).
28. O. L. Muskens, V. Giannini, J. A. Sánchez-Gil, and J. Gómez Rivas, "Optical scattering resonances of single and coupled dimer plasmonic nanoantennas," *Opt. Express* **15**(26), 17736–17746 (2007).
29. P. K. Jain, S. Eustis, and M. A. El-Sayed, "Plasmon coupling in nanorod assemblies: optical absorption, discrete dipole approximation simulation, and exciton-coupling model," *J. Phys. Chem. B* **110**(37), 18243–18253 (2006).
30. E. M. Hicks, S. Zou, G. C. Schatz, K. G. Spears, R. P. Van Duyne, L. Gunnarsson, T. Rindzevicius, B. Kasemo, and M. Käll, "Controlling plasmon line shapes through diffractive coupling in linear arrays of cylindrical nanoparticles fabricated by electron beam lithography," *Nano Lett.* **5**(6), 1065–1070 (2005).
31. B. Lamprecht, G. Schider, R. T. Lechner, H. Ditlbacher, J. R. Krenn, A. Leitner, and F. R. Aussenegg, "Metal nanoparticle gratings: influence of dipolar particle interaction on the plasmon resonance," *Phys. Rev. Lett.* **84**(20), 4721–4724 (2000).
32. N. Félidj, J. Aubard, G. Lévi, J. R. Krenn, G. Schider, A. Leitner, and F. R. Aussenegg, "Enhanced substrate-induced coupling in two-dimensional gold nanoparticle arrays," *Phys. Rev. B* **66**(24), 245407 (2002).
33. L. L. Zhao, K. L. Kelly, and G. C. Schatz, "The extinction spectra of silver nanoparticle arrays: influence of array structure on plasmon resonance wavelength and width," *J. Phys. Chem. B* **107**(30), 7343–7350 (2003).
34. C. L. Haynes, A. D. McFarland, L. L. Zhao, R. P. Van Duyne, G. C. Schatz, L. Gunnarsson, J. Prikulis, B. Kasemo, and M. Käll, "nanoparticle optics: the importance of radiative dipole coupling in two-dimensional nanoparticle arrays," *J. Phys. Chem. B* **107**(30), 7337–7342 (2003).
35. N. Félidj, G. Laurent, J. Aubard, G. Lévi, A. Hohenau, J. R. Krenn, and F. R. Aussenegg, "Grating-induced plasmon mode in gold nanoparticle arrays," *J. Chem. Phys.* **123**(22), 221103 (2005).
36. B. Auguié and W. L. Barnes, "Collective resonances in gold nanoparticle arrays," *Phys. Rev. Lett.* **101**(14), 143902 (2008).
37. J. Aizpurua, G. W. Bryant, L. J. Richter, F. J. García de Abajo, B. K. Kelley, and T. Mallouk, "Optical properties of coupled metallic nanorods for field-enhanced spectroscopy," *Phys. Rev. B* **71**(23), 235420 (2005).
38. R. Adato, A. A. Yanik, J. J. Amsden, D. L. Kaplan, F. G. Omenetto, M. K. Hong, S. Erramilli, and H. Altug, "Ultra-sensitive vibrational spectroscopy of protein monolayers with plasmonic nanoantenna arrays," *Proc. Natl. Acad. Sci. U.S.A.* **106**(46), 19227–19232 (2009).
39. W. Rechberger, A. Hohenau, A. Leitner, J. R. Krenn, B. Lamprecht, and F. R. Aussenegg, "Optical properties of two interacting gold nanoparticles," *Opt. Commun.* **220**(1–3), 137–141 (2003).
40. C. Sönnichsen, B. M. Reinhard, J. Liphardt, and A. P. Alivisatos, "A molecular ruler based on plasmon coupling of single gold and silver nanoparticles," *Nat. Biotechnol.* **23**(6), 741–745 (2005).
41. B. M. Reinhard, M. Siu, H. Agarwal, A. P. Alivisatos, and J. Liphardt, "Calibration of dynamic molecular rulers based on plasmon coupling between gold nanoparticles," *Nano Lett.* **5**(11), 2246–2252 (2005).

42. N. Yu, E. Cubukcu, L. Diehl, M. A. Belkin, K. B. Crozier, F. Capasso, D. Bour, S. Corzine, and G. Höfler, "Plasmonic quantum cascade laser antenna," *Appl. Phys. Lett.* **91**(17), 173113 (2007).
43. S. Zou, N. Janel, and G. C. Schatz, "Silver nanoparticle array structures that produce remarkably narrow plasmon lineshapes," *J. Chem. Phys.* **120**(23), 10871–10875 (2004).
44. S. Zou and G. C. Schatz, "Narrow plasmonic/photonic extinction and scattering line shapes for one and two dimensional silver nanoparticle arrays," *J. Chem. Phys.* **121**(24), 12606–12612 (2004).
45. F. Neubrech, D. Weber, D. Enders, T. Nagao, and A. Pucci, "Antenna sensing of surface phonon polaritons," *J. Phys. Chem. C* **114**(16), 7299–7301 (2010).
46. E. D. Palik, *Handbook of Optical Constants of Solids* (Academic Press, 1997).
47. Z. Chen, X. Li, A. Taflove, and V. Backman, "Backscattering enhancement of light by nanoparticles positioned in localized optical intensity peaks," *Appl. Opt.* **45**(4), 633–638 (2006).
48. V. E. Ferry, L. A. Sweatlock, D. Pacifici, and H. A. Atwater, "Plasmonic nanostructure design for efficient light coupling into solar cells," *Nano Lett.* **8**(12), 4391–4397 (2008).
49. K. Yee, "Numerical solution of initial boundary value problems involving Maxwell's equations in isotropic media," *IEEE Trans. Antenn. Propag.* **14**(3), 302–307 (1966).
50. A. Taflove, "Application of the finite-difference time-domain method to sinusoidal steady state electromagnetic penetration problems," *IEEE Trans. Electromagn. Compat.* **22**(3), 191–202 (1980).
51. B. T. Draine and P. J. Flatau, "Discrete-dipole approximation for periodic targets: theory and tests," *J. Opt. Soc. Am. A* **25**(11), 2693–2703 (2008).
52. P. Albella, F. Moreno, J. M. Saiz, and F. González, "Surface inspection by monitoring spectral shifts of localized plasmon resonances," *Opt. Express* **16**(17), 12872–12879 (2008).
53. F. Keilmann and R. Hillenbrand, "Near-field microscopy by elastic light scattering from a tip," *Philos. Transact. A Math. Phys. Eng. Sci.* **362**(1817), 787–805 (2004).
54. www.Neaspec.com
55. M. Schnell, A. García-Etxarri, A. J. Huber, K. Crozier, J. Aizpurua, and R. Hillenbrand, "Controlling the near-field oscillations of loaded plasmonic nanoantennas," *Nat. Photonics* **3**(5), 287–291 (2009).
56. M. Schnell, A. García-Etxarri, J. Alkorta, J. Aizpurua, and R. Hillenbrand, "Phase-resolved mapping of the near-field vector and polarization state in nanoscale antenna gaps," *Nano Lett.* **10**(9), 3524–3528 (2010).
57. N. Ocelic, A. Huber, and R. Hillenbrand, "Pseudoheterodyne detection for background-free near-field spectroscopy," *Appl. Phys. Lett.* **89**(10), 101124 (2006).
58. A. Pucci, F. Neubrech, J. Aizpurua, T. Cornelius, and M. Lamy de la Chapelle, "Electromagnetic nanowire resonances for field-enhanced spectroscopy," in *One-Dimensional Nanostructures*, Z. Wang, eds. (Springer, 2008), pp. 175–215.
59. M. Klevenz, F. Neubrech, R. Lovrincic, M. Jalochoowski, and A. Pucci, "Infrared resonances of self-assembled Pb nanorods," *Appl. Phys. Lett.* **92**(13), 133116 (2008).
60. C. Sönnichsen, T. Franzl, T. Wilk, G. von Plessen, J. Feldmann, O. Wilson, and P. Mulvaney, "Drastic reduction of plasmon damping in gold nanorods," *Phys. Rev. Lett.* **88**(7), 077402 (2002).
61. H. V. Chung, F. Neubrech, and A. Pucci, "Infrared spectroscopy of antenna resonances," *Proc. SPIE* **7394**, 73941E, 73941E-4 (2009).

---

## 1. Introduction

Since resonant excitation of plasmon polaritons (PP) in metallic nanostructures by light can yield considerable electromagnetic near-field enhancement, the optical properties of metal nanoparticles have been subject of many studies, for example [1,2]. This local field enhancement can be exploited for sensing applications like surface enhanced infrared (IR) spectroscopy (SEIRS) [3–8] or surface enhanced Raman scattering (SERS) [9–11], even making single molecule detection possible [12–14]. The sensitivity in SEIRS, for example, strongly depends on where the resonant excitation is spectrally located compared to the molecular vibration that is to be enhanced. Hence, the relation between spectral resonance position and geometrical properties of the nanostructures is essential for the optimization of sensing devices.

## 2. Antenna resonances in the infrared

In analogy to radio frequency (RF) antennas, resonantly excited nanostructures, especially in the IR, act as optical antennas that concentrate energy of electromagnetic radiation to a confined volume of sub wavelength scale. Thus, nanorods with  $\mu\text{m}$ -sized lengths  $L$ , which show plasmonic resonances in the IR spectral range [15–17], are termed nanoantennas. However, the simple  $\lambda/2$ -dipole behavior known from RF antennas, where the relationship between  $L$  and the resonant wavelength  $\lambda_{\text{res}}$  is given by  $2L = \lambda_{\text{res}}$ , does not hold for nanoantennas at optical (including IR) frequencies. Moreover, the finite penetration depth of

the light into the metal and the non-negligible diameter  $D$  of the antenna lead to the modified relation [18]

$$2L = c_2 [\lambda_{\text{res}} / \lambda_p] - c_1. \quad (1)$$

In this equation,  $\lambda_p$  denotes the plasma wavelength of the antenna's material whereas the coefficients  $c_1$  and  $c_2$  depend on  $D$  and on the static dielectric constant  $\epsilon_s$  of the surrounding medium. Basic assumption in this model is a high aspect ratio of the antenna ( $D \ll L$ ) and the metal is described as a free-electron gas according to the Drude model with negligible relaxation rate compared to photon frequencies. Since these conditions are sufficiently fulfilled for gold nanorods with  $L/D > 10$  in the mid IR [19], Eq. (1) can be used to describe the resonance behavior of isolated or at least *non-interacting* nanoantennas.

Instead of this equation in terms of  $\lambda_{\text{res}}$  and  $L$ , one can consider the dispersion relation  $\omega_{\text{res}}(k_{\text{pp}})$  between resonance frequency and wave vector of the PP wave;  $k_{\text{pp}} = \pi/L$  for the standing wave of the fundamental antenna resonance. The parameter  $c_1$  gives rise to a saturation behavior of the PP dispersion at higher wave vectors. Looking at  $\omega_{\text{res}}(k_{\text{pp}})$  makes easily obvious that higher  $\epsilon_s$  leads to a lower PP group velocity and a more rapid onset of saturation. That means,  $c_1$  becomes increasingly important for higher  $\epsilon_s$ , which was measured in [20].

### 3. Interaction effects in particle ensembles

Interaction between particles in multimers and in arrays of nanoantennas affects the optical properties of the system. The optical response therefore strongly depends on the separation distances, especially between nearest neighbor particles. Interaction effects were broadly analyzed experimentally and theoretically for different kinds of arrangements and shapes of particles. In addition to the investigation of coupling in dimers consisting of e.g. ellipsoids [21], spheres [22,23], nanodisks [24], nanorods [25,26], or nanoantennas [27,28], also many-particle systems like nanorod assemblies [29], linear arrays of nanocylinders [30], or two-dimensional (2D) nanoparticle arrays [31–36] have been subject of studies. It is important to note that all these studies focused on the visible spectral range while there are only a few dealing with the IR [20,37,38], where retardation can no more be neglected since an electromagnetic wave needs a not negligible time to travel from one rod end to the other. Because the rod lengths are similar to the wavelength, the Rayleigh limit is no more applicable to Mie scattering and extinction at resonance arises from absorption and scattering. Thus, the lineshape of the resonance curve is due to both the contributions, absorption and scattering, and we deal with the problem of resonant Mie scattering and asymmetric lines.

Two regimes of interaction between the antennas can be distinguished: the direct dipolar interaction in the near-field, which features a  $1/d^3$  dependence on the particle separation  $d$ , and the radiative coupling in the far-field, which varies as  $\exp(ikd)/d$  [30,34] with  $k$  being the wave vector of the emitted radiation that depends on  $\epsilon_s$ . The near-field interaction regime is relevant for very small  $d$ , whereas the long-range radiative coupling becomes important for  $d$  in the range of the wavelength in the surrounding medium. Therefore, in a system with nanoparticles on a substrate, its refractive index clearly determines the transition between near-field and radiative coupling.

Regarding the dipolar near-field coupling, a reduction of  $d$  between two spherical particles, for example, results in a strong red-shift of the resonance if the incident light is polarized parallel to the dimer axis. On the other hand, perpendicular polarization of the light leads to a moderate blue-shift for decreasing  $d$  [22,23,39]. This can be understood within the plasmon hybridization model [23] where an analogy to the formation of bonding and anti-bonding atomic orbitals exists. Similar behavior is observed for the longitudinal plasmon resonances of nanorod dimers: if the distance between the tip ends is reduced, a strong red-shift of the resonance occurs while a decrease of the distance perpendicular to the long rod axis results in a small shift of the resonance to shorter wavelengths [25,26]. In addition, it was found for elliptical dimers that the observed red-shift exponentially declines with increasing  $d$

and finally vanishes for  $d$  larger than approximately 2.5 times the short axis length [21]. This exponential decay is described as a plasmon ruler [24] and can be used to measure inter-particle distances in the presence of biological substances [40,41]. For elongated particles like nanorods, the tip-to-tip configuration yields very high electromagnetic field enhancements since the field can be confined in a very small gap between the tip ends [37,42].

The retarded radiative dipolar coupling, which depends on the phase shift between excitations of different particles, becomes especially important in ordered particle ensembles. Calculations for 2D square arrays of nanoparticles with one characteristic lattice constant in both lateral directions showed plasmon resonance blue-shifts with decreasing lattice constant as long as it is in the range of  $\lambda_{\text{res}}$  [33]. In addition, a narrowing of the collective plasmon resonance compared to that of a single particle is observed which is optimal for  $\lambda_{\text{res}}$  slightly bigger than the lattice constant [31,33,38]. This can be explained by the diffractive coupling (constructive interferences of emitted fields) of the particles and the resulting suppression of the radiation damping due to the collective scattering process. Moreover, the appearance of sharp spectral features was theoretically [43,44] and experimentally [20,30,36] analyzed and attributed to diffraction resulting from scattering by the periodic arrangement of the particles.

The difference between the above mentioned IR studies of Adato *et al.* [38] and the present work is pointed out now: In [38], nanorods on square lattices were investigated with respect to the influence of the lattice constant which was varied for fixed particle length. Consequently, by changing this lattice constant, the separation distance parallel (longitudinal) and perpendicular (transverse) to the long particle axis (in the case of elongated particles) is modified simultaneously. Since according to the symmetry of parallel-aligned nanorods on a substrate, the array is no more of quadratic symmetry, we investigated the effect of the longitudinal and transverse distances separately. In contrast to [38], special focus of this study is on the transverse coupling since it limits the nanoparticle density on a substrate for SEIRS applications.

#### 4. Materials and methods

The optical properties of 2D gold nanoantenna arrays in the IR range (2 – 12  $\mu\text{m}$ ) were investigated by far-field extinction spectroscopy and numerical simulations to relate resonance changes and near-field development to antenna distances. Furthermore, experimental insight into the properties of the near-field was obtained by scattering-type scanning near-field optical microscopy (s-SNOM). Besides that, the far-field behaviour of the Fano-type phonon-polariton feature of the  $\text{SiO}_2$  layer on the silicon wafer beneath the gold structures [45] supports the findings from the near-field mappings.

##### 4.1 Lithographic gold nanorods

Gold nanorod arrays were fabricated by electron beam lithography at the MANA Foundry station at NIMS, Tsukuba. Arrays with various distances between the rods and different rod lengths were prepared on two Si(111) floating zone wafers which slightly differed in the thin natural  $\text{SiO}_2$  layer (thickness of approximately 3 nm) covering the substrates. Details of the preparation process are described in [45]. The two samples will be called sample 1 and sample 2 in the remainder of the text. Each of them hosts different sets of nanoantennas with set-specific inter-antenna separation distances  $d_x$  (longitudinal) and  $d_y$  (transverse, see Fig. 1).

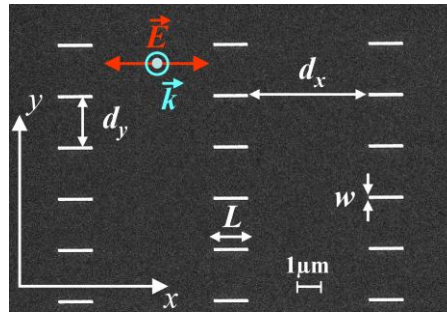


Fig. 1. SEM image of a part of a typical gold nanoantenna array on silicon as investigated. The set-specific separation distances  $d_x$  and  $d_y$  are indicated. The width  $w$  is about 120 nm for the rods of sample 1 and about 90 nm for the rods of sample 2, respectively. The height  $h$  is about 100 nm for all rods and the length  $L$  is varying in the different arrays between 370 nm and 2060 nm. The orientation of the electric field vector ( $\mathbf{E}$ ) is usually set parallel (as shown here) to the long rod axis to excite the longitudinal plasmon resonance. The incoming wave vector  $\mathbf{k}$  is always perpendicular to the substrate plane.

In the following, the notation  $d(x/y)$  will be used for a set with  $d_x = x \mu\text{m}$  and  $d_y = y \mu\text{m}$ . Furthermore, each set consists of several arrays featuring nanorods with rectangular cross-sections (width  $w \approx 120$  nm for sample 1 and  $w \approx 90$  nm for sample 2, with height  $h \approx 100$  nm for both) and the same length  $L$ . The dimensions of  $L$  and  $w$  were determined by statistical analysis based on scanning electron microscopy of each array and  $h$  is known from the evaporation process as well as from atomic force microscopy.

Since  $5 \mu\text{m}$  is large enough to minimize interaction between the individual nanorods in the spectral range of interest, set  $d(5/5)$  reflects the behavior of non-interacting antennas. Thus,  $d(5/5)$  acts as a reference for measurements in which  $d_x$  or  $d_y$  are reduced. On sample 1, two sets with reduced  $d_x$  [ $d(1/5)$  and  $d(0.04/5)$ ] and two with reduced  $d_y$  [ $d(5/2)$  and  $d(5/1)$ ] were prepared in order to identify possible interaction effects in longitudinal and transverse direction independently. Each set of sample 1 consists of 22 arrays with lengths  $L$  varying from 370 nm to 2050 nm. Whereas the rod length  $L$  was the main variation parameter on sample 1, sample 2 focuses on the variation of  $d_y$ . Here, 8 different sets with only 5 distinct lengths (620 nm, 820 nm, 1030 nm, 1550 nm, and 2060 nm) exist:  $d(5/5)$ ,  $d(5/2)$ ,  $d(5/1.5)$ ,  $d(5/1)$ ,  $d(5/0.75)$ ,  $d(5/0.5)$ ,  $d(5/0.25)$ , and  $d(5/0.1)$ .

#### 4.2 Microscopic infrared spectroscopy

Far-field IR spectroscopic measurements were performed with an IR microscope (Bruker Hyperion 1000) coupled to a Fourier-Transform IR spectrometer (Bruker Tensor 27 with a  $\text{LN}_2$  cooled mercury-cadmium-telluride detector, optical path purged with dried air). IR transmittance spectra were taken at normal incidence with a numerical aperture of  $\text{NA} = 0.52$ . The measured IR spectra of the nanorods on the substrate were normalized to those of a bare substrate area taken at least  $50 \mu\text{m}$  away from any rod to eliminate all background features. A circular aperture with a diameter of  $33.3 \mu\text{m}$  in the focal plane of the IR microscope was used and all spectra were acquired with at least 3000 scans at a resolution of 4 or  $8 \text{ cm}^{-1}$  in the spectral range from  $700$  to  $7000 \text{ cm}^{-1}$  ( $14.3 \mu\text{m}$  to  $1.4 \mu\text{m}$ ). The IR beam passes an IR polarizer (before the sample) that was in most cases aligned parallel to the long rod axis (see Fig. 1).

#### 4.3 Numerical simulations

In first approximation, numerical solution of the IR extinction for the systems described above has been obtained by solving Maxwell's equations for a plane wave incident on the exact geometry of an individual gold nanoantenna (isolated nanorod in the remainder of the text) and an individual nanoantenna pair (dimer in the following) on a silicon wafer with 3 nm oxide. Note that this dimer model satisfactorily reproduces the spectral changes induced by

the decreasing separation distances. In addition, to obtain better agreement with the experimental results, some spectra were simulated by solving Maxwell's equations for an incident Gaussian beam (diameter of 40  $\mu\text{m}$ ) illuminating gold nanoantenna arrays, consisting of a large number of antenna units on a silicon wafer with 3 nm oxide with the same geometrical parameters as in the experiments.

The simulations have been performed with use of finite-difference time-domain software (Lumerical) using optical data of Palik's reference book [46]. This numerical method is broadly established in computational electromagnetism to calculate the optical response of different nanostructures [47,48]. It consists of a direct implementation of the Maxwell time-dependent curl equations to solve the temporal variations of electromagnetic waves within a finite space that contains objects of arbitrary shape and properties (perfectly matched layers were used as boundary conditions). In practice, the space including the scatterer is discretized into a grid that contains the basic element of this discretization, the Yee cell [49,50]. The precision of the results depend both on the number of the cells used in the simulation, as well as on the appropriate selection of the simulation time. The presented results are fully converged, thus they can be considered an exact solution of Maxwell's equations. Additionally, some of the results shown here have been tested with another solving method, the discrete dipole approximation (DDA) [51,52], producing very good agreement.

#### 4.4 Infrared scattering-type scanning near-field optical microscopy (s-SNOM) [53]

Near-field imaging was performed with a commercial s-SNOM (Neaspec NeaSNOM [54]). It is based on an atomic force microscope (AFM), where dielectric silicon tips are employed as scattering near-field probes [55,56]. Both tip and antenna are illuminated with s-polarized radiation from a CO<sub>2</sub> laser ( $\lambda = 11.1 \mu\text{m}$ ) under an angle of 60° from the surface normal. The incident polarization is parallel to the long axis of the antennas. The light scattered by the tip is detected with a pseudo-heterodyne interferometer [57]. By selecting the p-polarized tip-scattered light with a polarizer, the amplitude of the vertical near-field component  $E_z$  was recorded [56].

## 5. Results and discussion

First, the effect of changing the longitudinal separation distance  $d_x$  on the IR extinction spectra is shown by means of the far-field spectroscopic measurements of the sets  $d(5/5)$ ,  $d(1/5)$ , and  $d(0.04/5)$  on sample 1. After that, the change of the spectra due to the variation of the transverse separation distance  $d_y$  is analyzed. Here, the far-field measurements of  $d(5/5)$ ,  $d(5/2)$ , and  $d(5/1)$  on sample 1 as well as all measurements of the sets on sample 2 are used. Finally, the relative changes of the optical properties of the interacting nanorod arrays with respect to the non-interacting reference arrays are discussed for the both cases, the longitudinal and the transverse coupling. In addition, experimental results are compared to numerical simulations.

### 5.1 Longitudinal interaction

Figure 2(a) shows a selection of relative transmittance spectra of three different arrays (all on sample 1) with similar rod lengths (820 nm) but different  $d_x$  ( $d_y = 5 \mu\text{m}$  is kept constant). The fundamental dipolar resonances can be observed at around  $\lambda \approx 5 \mu\text{m}$ . Since the rod density in the three arrays differs, varying numbers of rods [as given in Fig. 2(a)] contribute to each spectrum. To account for that in Fig. 2(b), we calculate the ratio of extinction cross-section ( $\sigma_{\text{ext}}$ ) to geometrical cross-section ( $\sigma_{\text{geo}} = L w$ ) and normalize it to one nanorod (referred to as  $\sigma_{\text{ext}}(\lambda)/\sigma_{\text{geo}}$  in the remainder of the text) in a similar way to previous works [15,16,58,59]. At around  $\lambda = 2.6 \mu\text{m}$  in the dotted red curves in Fig. 2(a) and 2(b), the second order plasmonic excitation [19] weakly appears. Besides that, the small feature between  $\lambda = 8 \mu\text{m}$  and  $\lambda = 9 \mu\text{m}$  is attributed to the excitation of a thin-film surface phonon-polariton in the natural SiO<sub>2</sub> layer covering the Si substrate [45]. It is important to note that this feature is related to a wave vector parallel to the substrate surface and shows up in case of sufficiently strong near-field components (near the nanorod ends).

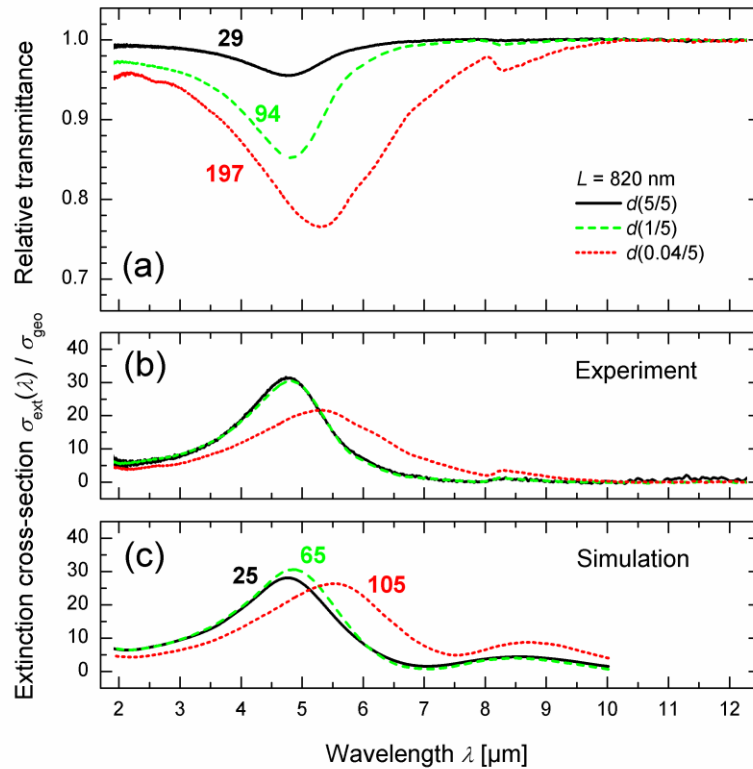


Fig. 2. (a) Measured relative IR transmittance spectra and (b) corresponding extinction cross-sections per nanorod normalized to geometric cross-section  $[\sigma_{\text{ext}}(\lambda)/\sigma_{\text{geo}}]$  for the nanorod arrays  $d(5/5)$ ,  $d(1/5)$ , and  $d(0.04/5)$  with  $L \approx 820$  nm,  $w \approx 120$  nm, and  $h \approx 100$  nm. The orientation of the electric field vector was always parallel to the long rod axis. The numbers in (a) give the approximate quantity of rods which contribute to the corresponding signals. (c) Numerical simulations of  $\sigma_{\text{ext}}(\lambda)/\sigma_{\text{geo}}$  per nanorod for nanoantenna arrays with the same geometrical dimensions as the experimentally investigated nanorods. The numbers indicate the quantity of rods used in the calculations until convergence was achieved.

The simulated extinction spectra in Fig. 2(c), which were performed for three arrays in a configuration similar to the experimental situation of sample 1 (only the total number of rods is differing), satisfactorily correspond to the experimental spectra in Fig. 2(b). Deviations concern the phonon-polariton feature that is broader than in the experiment. In addition, interference with the tail of the plasmon resonance makes it looking like shifted in the calculation. The most probable reason for this observed spectral difference is that the  $\text{SiO}_2$  IR optical textbook data and the ideal  $\text{SiO}_2/\text{Si}$  interface model used in the simulation do not exactly describe the real optical response of the thin natural oxide layer with non-ideal stoichiometry.

It should be mentioned that the quality factors  $Q$  (ratio between resonance frequency and full width at half maximum) of the antenna resonances shown here range between 2 and 3. These values are relatively small compared to that of gold nanoantennas in the visible (e.g.  $Q \approx 20$  reported in [60]). This is related to the much stronger radiative damping in the IR where electronic damping gives a rather weak, but non-negligible effect [16,61].

Our main focus is to understand how interaction within the array changes the characteristic properties of the fundamental resonance such as  $\lambda_{\text{res}}$ ,  $Q$  and  $\sigma_{\text{ext}}(\lambda_{\text{res}})/\sigma_{\text{geo}}$ . First concentrating on the spectral position of the resonance, Fig. 3(a) shows  $\lambda_{\text{res}}$  versus the rod length  $L$  for the three sets  $d(5/5)$ ,  $d(1/5)$ , and  $d(0.04/5)$  featuring different  $d_x$ . The relation between  $L$  and  $\lambda_{\text{res}}$  is important for the optimization of sensing applications in SEIRA where  $\lambda_{\text{res}}$  has to match the

wavelength of the IR active vibration being sensed [5]. For non-interacting antennas with aspect ratios bigger than 10, the spectral position of the resonance,  $\lambda_{\text{res}}(L)$ , can be described by L. Novotny's approximation [Eq. (1)] using the effective radius  $R$  according to the rod's cross-section and the plasma wavelength  $\lambda_p$  of gold as fixed inputs [16,19]. Hence, the experimental data for  $d_x = 5 \mu\text{m}$  and  $L > 1 \mu\text{m}$  [full black circles in Fig. 3(a)] nicely follows Eq. (1) with  $c_1 = 268 \text{ nm}$  and  $c_2 = 54 \text{ nm}$  for an effective dielectric background of 6.2 that corresponds to a nearly 1:1 mixture of the dielectric constants of silicon (11.7) and air. However, this result for the dielectric constant should not be over-interpreted since the slope of the linear relation between  $L$  and  $\lambda_{\text{res}}$  in our experiments turned out to be affected by details of the interface layers between gold and substrate. Nevertheless, our simulation results from *isolated* gold nanorods ( $w = 120 \text{ nm}$ ,  $h = 100 \text{ nm}$ ) placed on 3 nm thin  $\text{SiO}_2$  on silicon [full black circles in Fig. 3(b)] are in very good agreement with the measurements of  $d(5/5)$  and correspond to a dielectric background of 6.4 if compared to Eq. (1). The small difference could be due to the assumption of ideal interfaces in the simulations. However, the good agreement between the measurements of arrays and the simulation of isolated nanorods supports the assumption that interaction is minimal in the case of set  $d(5/5)$ .

Clearly visible from Fig. 2 as well as from Fig. 3 is the red-shift of  $\lambda_{\text{res}}$  for  $d_x = 40 \text{ nm}$  while for  $d_x = 1 \mu\text{m}$ , the results are nearly the same as for  $d_x = 5 \mu\text{m}$ . Note that the simulated resonances shown in Fig. 3(b) (open green squares and open red triangles) are performed for nanorod dimers since they quite accurately reproduce the observed spectral changes [there is only a small difference between the dimer and the array simulation (open blue diamond) with  $L = 820 \text{ nm}$ ]. The data of Fig. 3 will be discussed in more detail in Sec. 5.3.

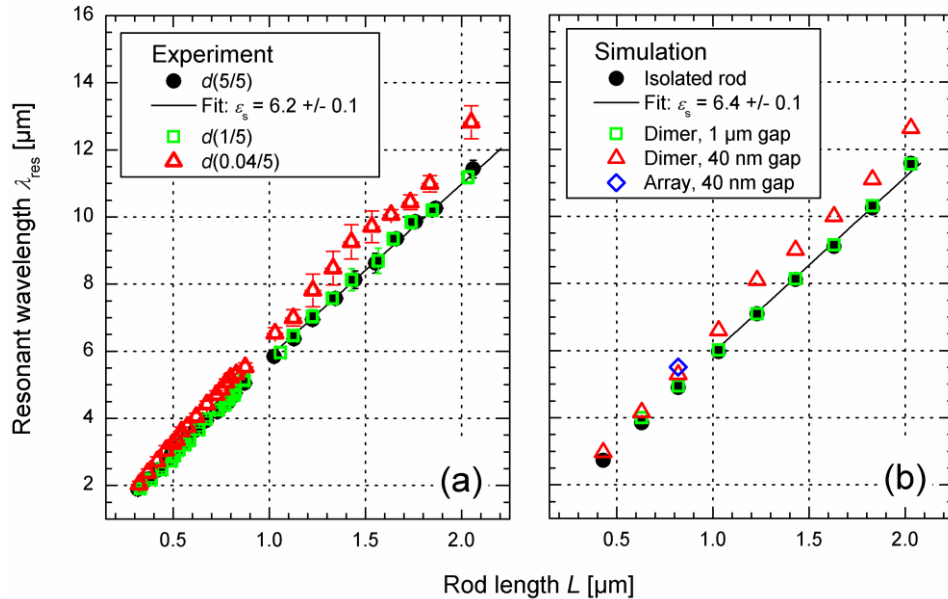


Fig. 3. Optical wavelength of the fundamental plasmonic resonance ( $\lambda_{\text{res}}$ ) versus rod length  $L$  for different longitudinal distances  $d_x$ , (a) experiment, (b) simulation. The solid lines show fits according to Eq. (1) using the fixed inputs  $R = 61 \text{ nm}$  and  $\lambda_p = 138 \text{ nm}$ . The simulated resonances in this graph are obtained for dimer rods since they represent quite accurately the longitudinal coupling in full arrays for these separation distances.

## 5.2 Transverse interaction

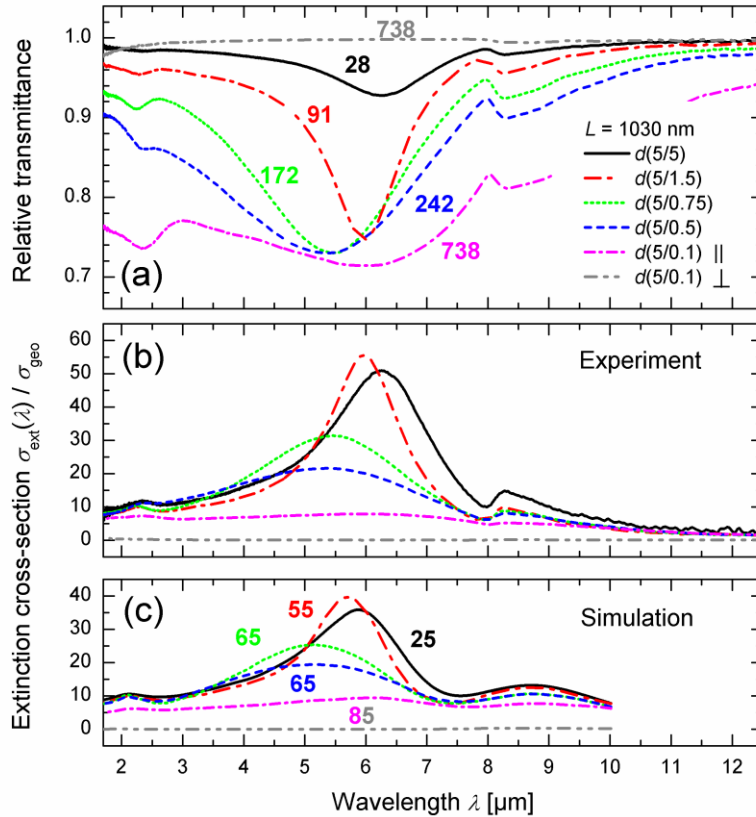


Fig. 4. As Fig. 2, but  $L = 1030$  nm,  $w = 90$  nm,  $d_x = 5$   $\mu\text{m}$  and  $d_y$  according to the values given in (a). In all spectra, the polarization of the electric field is parallel to the long rod axis except for the grey curve which shows a spectrum with perpendicular ( $\perp$ ) polarization of  $d(5/0.1)$  for comparison. The small feature between  $\lambda = 8$   $\mu\text{m}$  and  $\lambda = 9$   $\mu\text{m}$  is due to the surface phonon-polariton in the natural  $\text{SiO}_2$  layer covering the Si substrate. The simulations shown in (c) were performed for nanorod arrays (total number of rods given in the figure) with same  $L$ ,  $h$ , and  $d_y$  as in the experimental situation (a). The only difference between simulation and experiment, besides the total number of rods, is the rod width  $w$  which was 120 nm for the simulations.

Now we turn the focus of our study to the effect of changes of the transverse separation distance  $d_y$  for constant  $d_x = 5$   $\mu\text{m}$ . Figure 4(a) and 4(b) shows IR transmittance spectra and the corresponding values of  $\sigma_{\text{ext}}(\lambda)/\sigma_{\text{geo}}$  for nanorod arrays with  $L = 1030$  nm and different  $d_y$ . Obviously, significant differences occur for different  $d_y$ . Interestingly, the extinction spectrum of  $d(5/1.5)$  [red curve in Fig. 4(b)] is narrower and features a higher maximum extinction than that of the reference array  $d(5/5)$  (black curve). Since a distance of 1.5  $\mu\text{m}$  is rather large, one can exclude dominant near-field dipolar coupling and this effect can be attributed to radiative dipolar coupling. Furthermore, the spectra broaden very much as  $d_y$  decreases and the extinction cross-section becomes almost a flat “background” for  $d_y = 100$  nm [pink curve in Fig. 4(b)]. However, this value is still clearly above the geometric cross-section. Clearly visible on that “background” is a higher order antenna excitation at about  $\lambda = 2.5$   $\mu\text{m}$  that can be attributed to a red-shifted third order resonance. Since the broad resonances of the various orders overlap and therefore are coupled by dipolar interaction, this coupling in principle should lead to new kinds of mixed excitations with new positions for extinction maxima, which may also explain the red-shift of the fundamental resonance for  $d_y = 100$  nm (pink curve) compared to  $d_y = 500$  nm (blue curve) in Fig. 4(a). Moreover, no extinction could be

observed for polarization perpendicular to the long rod axis [grey curve in Fig. 4(b)], which is confirmed by the simulation [grey curve in Fig. 4(c)].

Note that there is a qualitatively good agreement between the tendencies of the main plasmonic resonances of the simulations shown in Fig. 4(c) and experimental data shown in Fig. 4(b). Since the simulations were performed for arrays on an *ideal* SiO<sub>2</sub> layer, deviations between experiment and calculation occur concerning the shape of the phonon-polariton signal. In addition, the discrepancies in the total values of  $\sigma_{\text{ext}}(\lambda)/\sigma_{\text{geo}}$  are most probably due to the different rod width  $w$  used in the simulations (120 nm compared to 90 nm in the experiments). However, the relative change of the optical properties is not affected by the different rod width  $w$ , as we will see in Sec. 5.3.

### 5.3 Discussion of interaction effects

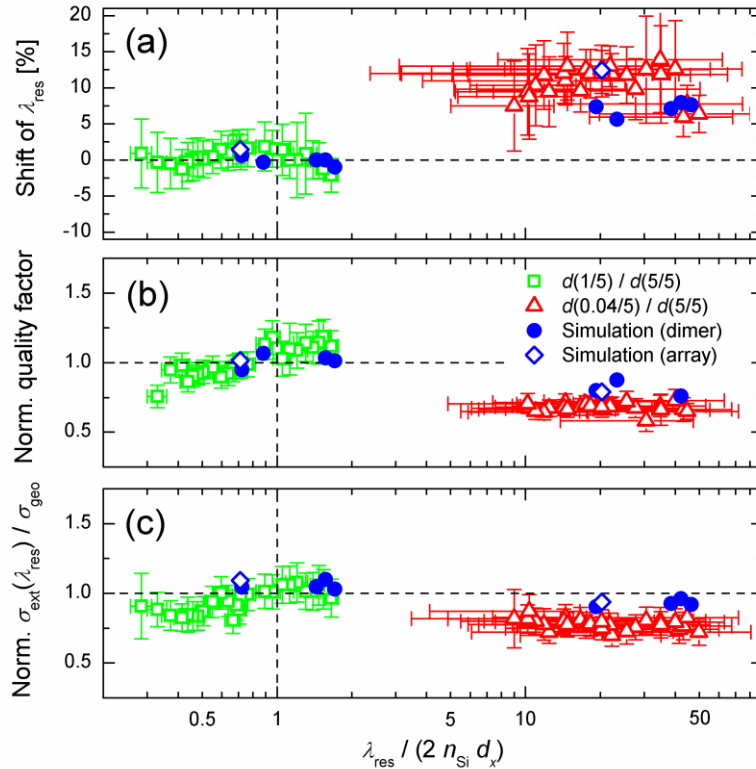


Fig. 5. (a) Shift of the spectral resonance position of the sets  $d(1/5)$  and  $d(0.04/5)$  with respect to the reference set  $d(5/5)$ . The full blue circles are the results obtained from the numerical simulations of dimers whereas the open blue diamonds are obtained from the simulations of arrays, respectively. In addition, the relative change of the quality factor  $Q$  (b) and the maximum extinction at resonance  $\sigma_{\text{ext}}(\lambda_{\text{res}})/\sigma_{\text{geo}}$  (c) compared to  $d(5/5)$  are shown. The abscissa represents the ratio between one half of the resonant wavelength in silicon  $[\lambda_{\text{res}}/(2n_{\text{Si}})]$  and separation distance  $d_x$  (see text). All experimental results originate from sample 1.

Figure 5 represents the relative *changes* of the characteristic resonance parameters  $\lambda_{\text{res}}$ ,  $Q$  and  $\sigma_{\text{ext}}(\lambda_{\text{res}})/\sigma_{\text{geo}}$  of the arrays with reduced longitudinal distance  $d_x$  compared to the non-interacting reference arrays  $d(5/5)$ . On the ordinate scale, Fig. 5(a) shows the relative shift of  $\lambda_{\text{res}}$  of the two arrays  $d(1/5)$  (open green squares) and  $d(0.04/5)$  (open red triangles) with respect to  $d(5/5)$ . Any positive values indicate a red-shift of the resonance while negative values accordingly represent a blue-shift. Note that the data shown here in Fig. 5(a) is essentially the same as the data in Fig. 3, only in a different kind of representation. Because of the substrate polarizability, the wavelength in the substrate is the crucial quantity when

interaction between plasmonic particles is considered [20,31,38]. Accordingly, in Fig. 5, the logarithmic abscissa indicates the ratio between one half of the resonant wavelength in silicon [ $\lambda_{\text{res}}/(2n_{\text{Si}})$  with  $n_{\text{Si}}$  the refractive index of silicon] and  $d_x$ . Here, a value of one represents the condition of constructive interference, as illustrated in Fig. 6(a).

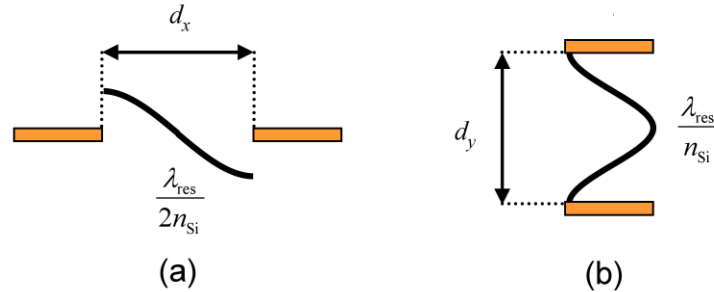


Fig. 6. Constructive interference conditions for (a) longitudinal and (b) transverse coupling. In the first case, one half of the wavelength in the substrate ( $\lambda_{\text{res}}/2n_{\text{Si}}$ ) has to match the longitudinal separation distance  $d_x$ , whereas in the latter one, one full wavelength in the substrate ( $\lambda_{\text{res}}/n_{\text{Si}}$ ) equals the transverse separation distance  $d_y$ .

The relative changes of  $Q$  and  $\sigma_{\text{ext}}(\lambda_{\text{res}})/\sigma_{\text{geo}}$  with respect to  $d(5/5)$  are shown in Fig. 5(b) and 5(c) to more clearly present the information of line shape and extinction change in the different cases. The situation with the narrow 40 nm gap (open red triangles) yields lower values of  $Q$  and  $\sigma_{\text{ext}}(\lambda_{\text{res}})/\sigma_{\text{geo}}$  for all  $L$  under investigation compared to the  $d(5/5)$  arrays. One has to notice that these lower far-field values indicate a lower amount of scattering out of the incident photon wave vector direction and do not necessarily mean lower near-field intensity. At sufficiently small  $d_x$ , the near-field dipolar coupling becomes the dominating interaction. For example, for gold nanorod dimers ( $L = 200$  nm,  $R = 40$  nm) surrounded by vacuum in the near IR, the separation distance threshold was calculated to be at about 100 nm [37]. Moreover, the spectral red-shift for small  $d_x$  as well as the reduced values for  $Q$  and  $\sigma_{\text{ext}}(\lambda_{\text{res}})/\sigma_{\text{geo}}$  can be understood by looking at a coupled dipole model including retardation [37]. It predicts that the decline of the far-field intensity and the consequential broadening of the resonance are evidences for interaction. The same studies show near-field increase for small  $d_x$ . Complementarily, SEIRS measurements [7] also indicate increased electromagnetic field enhancement for coupled nanorods in tip-to-tip configuration.

Moreover, the experimental data in Fig. 5 shows that there is no significant far-field interaction effect for  $d_x = 1$   $\mu\text{m}$  (open green squares) except a slight increase of  $Q$  and  $\sigma_{\text{ext}}(\lambda_{\text{res}})/\sigma_{\text{geo}}$  at around  $\lambda_{\text{res}}/(2n_{\text{Si}}d_x) \approx 1$ . For application to SEIRS with antenna arrays, the findings for the variation in  $d_x$  mean that the rod density on a substrate (and hence the signal-to-noise ratio) can be increased by reducing the longitudinal distance  $d_x$  close to  $\lambda_{\text{res}}/(4n_s)$ , here  $n_s$  for the refractive index of the substrate, without changing the properties of the plasmonic resonance very much.

The data from the simulations of dimers (full blue circles) nicely fits to the experimental data of  $d(1/5)$ . In addition, only a very small difference is present between the dimer and array simulation (open blue diamond) at around  $\lambda_{\text{res}}/(2n_{\text{Si}}d_x) = 0.7$ . This again indicates that there is only a small far-field interaction effect for  $d_x = 1$   $\mu\text{m}$ . In contrast, the shift of the resonance is slightly bigger for the array simulation compared to the dimer simulation at  $\lambda_{\text{res}}/(2n_{\text{Si}}d_x) = 20$ . This increased red-shift can be explained by the fact that each rod has two direct neighbors in the case of an array which leads to a more decreased intra-rod restoring force compared to the dimer case where only one direct neighbor exists. Hence, the simulation of arrays better fits to the experimental results even though the dimer model already gives qualitatively good agreement.

Figure 7 summarizes all spectral changes of  $\lambda_{\text{res}}$  (a),  $Q$  (b), and  $\sigma_{\text{ext}}(\lambda_{\text{res}})/\sigma_{\text{geo}}$  (c) with respect to  $d(5/5)$  for decreasing  $d_y$  in the same manner as Fig. 5. The only difference in

representation is that the abscissa relates one full wavelength in the substrate ( $\lambda_{\text{res}}/n_{\text{Si}}$ ) to the transverse separation distance  $d_y$  to reflect the constructive interference condition at  $\lambda_{\text{res}}/(n_{\text{Si}}d_y) = 1$  as illustrated in Fig. 6(b). The open blue squares originate from the sets  $d(5/2)$  and  $d(5/1)$  on sample 1 whereas the open black circles represent the data of all sets of sample 2. Although the relation of  $\lambda_{\text{res}}(L)$  is slightly different for the sets  $d(5/1)$ ,  $d(5/2)$ , and  $d(5/5)$  on the two samples (because of different interface layers between gold and substrate and different rod widths  $w$ , not shown here), the *relative change* of  $d(5/1)$  and  $d(5/2)$  when compared to the corresponding reference set  $d(5/5)$  of sample 1 and 2, respectively, is the same [see Fig. 7(a)].

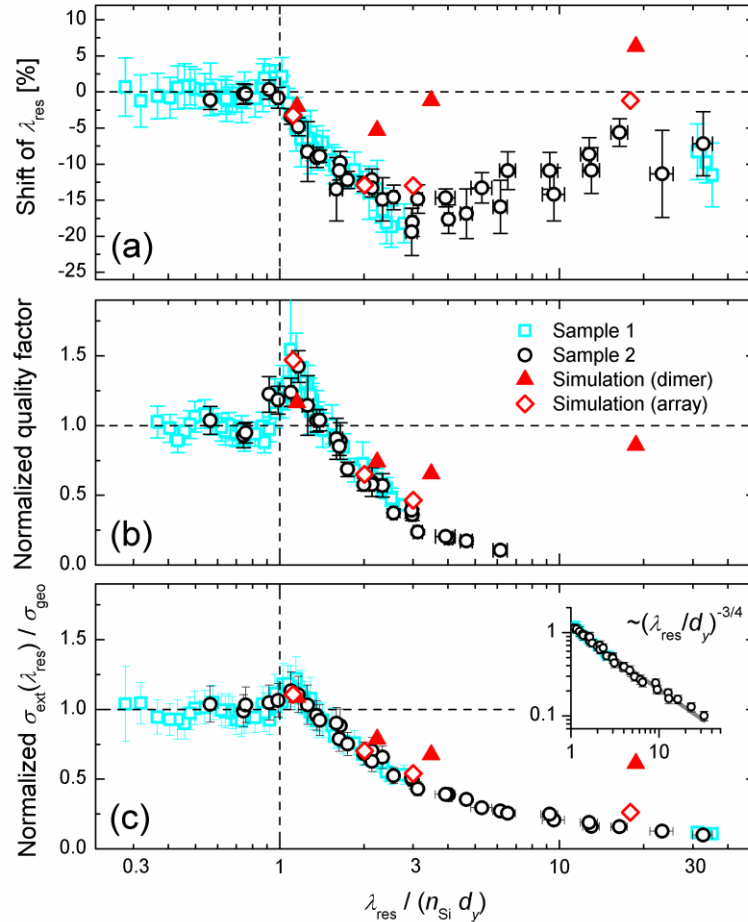


Fig. 7. As Fig. 5 but for different separation distances in transverse direction. Note that the abscissa relates one full resonant wavelength in the substrate to the transverse separation distance  $d_y$ . The relative shift of  $\lambda_{\text{res}}$  (a) as well as the relative changes of  $Q$  (b) and  $\sigma_{\text{ext}}(\lambda_{\text{res}})/\sigma_{\text{geo}}$  (c) with respect to the reference set  $d(5/5)$  are shown for the sets  $d(5/1)$  and  $d(5/2)$  on sample 1 ( $w = 120$  nm,  $h = 100$  nm) and all sets on sample 2 ( $w = 90$  nm,  $h = 100$  nm). The full red triangles are data from simulations where nanorod dimers are compared to isolated nanorods. In addition, simulations of nanorod arrays (open red diamonds) are shown for comparison. The inset in (c) shows the same data as in (c) but with a logarithmic ordinate scale. As indicated by the solid grey line, the decrease of  $\sigma_{\text{ext}}(\lambda_{\text{res}})/\sigma_{\text{geo}}$  is proportional to  $(\lambda_{\text{res}}/d_y)^{-3/4}$ .

From Fig. 7 it is obvious that a qualitative change in dipolar interaction occurs at  $\lambda_{\text{res}}/(n_{\text{Si}}d_y) \approx 1$ , the constructive interference condition [Fig. 6(b)]: blue-shift of the resonance accompanied by strong broadening and strongly decreased values of  $\sigma_{\text{ext}}(\lambda_{\text{res}})/\sigma_{\text{geo}}$  are observed towards larger  $\lambda_{\text{res}}/(n_{\text{Si}}d_y)$  ratios. For smaller ratios  $\lambda_{\text{res}}/(n_{\text{Si}}d_y)$ , one can detect some small oscillatory behavior from various far-field interference orders, clearly more pronounced than

for the separation distance in longitudinal direction (Fig. 5), and with a different relationship to the separation distance. In Fig. 7, deviations between experiments (arrays) and the simulations of dimers (solid red triangles) are more pronounced as the transverse distance becomes smaller. These differences demonstrate the effect of the missing neighbors in the simulation where mainly the near-field in the gap between the two rods is modified by interaction while in the array the rods have modified near-fields on both sides. To account for that, we also performed simulations with an increasing number of interacting rods (array simulations, open red diamonds) and nearly perfect agreement with the experimental results is obtained. Nevertheless, also the simple interacting dimer model explains and predicts very satisfactorily the main experimental results.

Considering the results above, it is possible to identify the optimum geometry for maximum  $Q$  and plasmonic resonances only marginally shifted from the position of a non-interacting antenna:  $0.5 \leq \lambda_{\text{res}}/(2n_{\text{Si}}d_x) \leq 2$  and  $\lambda_{\text{res}}/(n_{\text{Si}}d_y)$  slightly bigger than one, see Figs. 5 and 7. This is in reasonable agreement with the work of R. Adato *et al.* [38] and accounts for the fact that there are different conditions for constructive interference in radiative coupling for the two directions (Fig. 6). In longitudinal direction, resonances are only slightly sharper in a range around  $\lambda_{\text{res}}/(2n_{\text{Si}}d_x) \approx 1$  whereas in transverse direction, a significant constructive first order interference appears for  $\lambda_{\text{res}}/(n_{\text{Si}}d_y) \approx 1$ . The anisotropy of the far-field interaction in the nanorod array is influenced by the anisotropic emission pattern of an oscillating dipole: most of the electromagnetic power is radiated perpendicular to the oscillation axis and thus the change in  $d_y$  gives stronger interference effects. Strong anisotropy is also measured for the near-field coupling range of gap sizes (compare Figs. 5 and 7 for values on the abscissa bigger than one). Significant blue-shift, decrease of the normalized extinction cross-sections at resonance maximum and extraordinary broadening are only observed for transverse gap size decrease below  $\lambda_{\text{res}}/n_{\text{Si}}$ . Interestingly, the decrease of  $\sigma_{\text{ext}}(\lambda_{\text{res}})/\sigma_{\text{geo}}$  seems to be proportional to  $(\lambda_{\text{res}}/d_y)^{-3/4}$ , as the inset of Fig. 7(c) shows. Coupling of the antennas over a small  $d_y$  (of about 100 nm in our study) disturbs the confinement of resonant near-field at the nanorod ends, very differently compared to the increased confinement at small  $d_x$ .

To provide direct experimental evidence of the near-field behaviour with transverse coupling, we performed near-field mapping of selected antenna arrays employing s-SNOM at  $\lambda = 11.1 \mu\text{m}$  wavelength. Figure 8(a)–8(e) shows the amplitude of the vertical near-field component  $E_z$  for a set of parallel 1.5  $\mu\text{m}$ -long gold nanorods, where the transverse spacing  $d_y$  varies from 5  $\mu\text{m}$  to 100 nm. To compare the near-field amplitude signals of the different transverse separations, all the images were taken with the same tip, the same mapping parameters, and the same laser alignment. In Fig. 8(a), ( $d_y = 5 \mu\text{m}$ ), a typical dipole pattern is observed: two bright spots at the rod extremities [55], which proves enhanced near-field amplitudes. With decreasing  $d_y$ , the amplitude signals decrease, nearly vanishing for  $d_y = 100 \text{ nm}$  [Fig. 8(e)].

In addition to the experimental results, FDTD simulations were carried out for the near-fields around the nanoantennas [Fig. 8(f)–8(j)] to support the experimental findings. And in fact, qualitative good agreement between experiment and simulation is obtained. The two image series indeed corroborate the assumption made from the far-field spectroscopy in Figs. 5 and 7, namely that the near-field in the long wavelength region of the spectrum decreases due to transverse near-field coupling. The decrease of the near-field intensity is also experimentally visible in Fig. 4(b), where the extinction cross-section for  $d_y = 100 \text{ nm}$  (pink curve) shows a weaker signal from the  $\text{SiO}_2$  phonon-polariton feature. From these findings and from the strong broadening and weakening of the plasmonic resonance spectrum, one can conclude that a decrease of the transverse distance  $d_y$  below  $\lambda_{\text{res}}/n_{\text{Si}}$  is not beneficial for SEIRS.

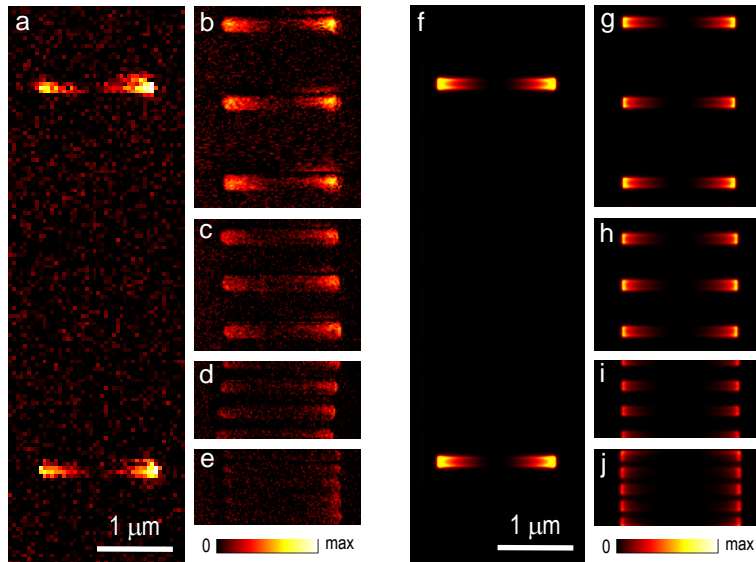


Fig. 8. Near-field amplitude images obtained by s-SNOM of 1.5  $\mu\text{m}$  long gold nanorods with varying transverse distances  $d_t$ : 5  $\mu\text{m}$  (a), 1  $\mu\text{m}$  (b), 500 nm (c), 250 nm (d), and 100 nm (e). All images are obtained at a wavelength  $\lambda = 11.1 \mu\text{m}$ . For comparison, (f) to (j) show simulations of the near-field for the same structures as (a) to (e). In both cases, the transverse near-field coupling is increased from (a) to (e) and (f) to (j), respectively, but the amplitude of the near-field decreases.

## 6. Summary

We investigated the different influence of inter-antenna separation distances in transverse and longitudinal directions in ordered rectangular arrays of “one-dimensional” plasmonic nanoantennas. From experimental IR investigations of lithographic gold nanorod arrays on silicon wafers and numerical simulations, we obtained optimum array parameters for maximum quality factor (in far-field extinction), namely longitudinal and transverse distances according to the respective first constructive interference conditions. These conditions are important for the selectivity of an application. In SEIRS, however, the near-field enhancement of plasmonic resonances and the number of sites featuring that field enhancement have to be maximized. For a SEIRS array we therefore propose very small longitudinal gaps and transverse separation distances according to the first constructive interference condition with the gap size equal to the resonant wavelength in the substrate. Concerning the array design, it has to be considered that the longitudinal near-field coupling strongly changes the resonance position of the plasmonic resonance and therefore the antenna length needs to be adjusted to the vibrational frequencies of interest.

## Acknowledgments

Financial support by the European project NANOANTENNA (HEALTH-F5-2009-241818), by the Strategic International Cooperative Program through the Japan Science and Technology Agency and the German Science Foundation (DFG PU193/9-1), by the Heidelberg Graduate School of Fundamental Physics, by the National project FIS-2010-19609-C02-02 from the Spanish Ministry of Science and Innovation, and by the ETORTEK project inanoGUNE from the Department of Industry of the Basque Government is gratefully acknowledged.